

Raman spectroscopy study of the slow order–order transformation of deuterium atoms: Ice XIX decay and ice XV formation

Cite as: J. Chem. Phys. **156**, 154507 (2022); <https://doi.org/10.1063/5.0087592>

Submitted: 07 February 2022 • Accepted: 31 March 2022 • Accepted Manuscript Online: 31 March 2022
• Published Online: 19 April 2022

 Alexander V. Thoeny,  Iside S. Parrichini,  Tobias M. Gasser, et al.

COLLECTIONS

Paper published as part of the special topic on [Slow Dynamics](#)



View Online



Export Citation



CrossMark

ARTICLES YOU MAY BE INTERESTED IN

[Advances in the experimental exploration of water's phase diagram](#)

The Journal of Chemical Physics **150**, 060901 (2019); <https://doi.org/10.1063/1.5085163>

[Ab initio metadynamics determination of temperature-dependent free-energy landscape in ultrasmall silver clusters](#)

The Journal of Chemical Physics **156**, 154301 (2022); <https://doi.org/10.1063/5.0082332>

[Explaining reaction coordinates of alanine dipeptide isomerization obtained from deep neural networks using Explainable Artificial Intelligence \(XAI\)](#)

The Journal of Chemical Physics **156**, 154108 (2022); <https://doi.org/10.1063/5.0087310>

Lock-in Amplifiers
up to 600 MHz



Zurich
Instruments



Raman spectroscopy study of the slow order–order transformation of deuterium atoms: Ice XIX decay and ice XV formation

Cite as: *J. Chem. Phys.* **156**, 154507 (2022); doi: [10.1063/5.0087592](https://doi.org/10.1063/5.0087592)

Submitted: 7 February 2022 • Accepted: 31 March 2022 •

Published Online: 19 April 2022



View Online



Export Citation



CrossMark

Alexander V. Thoeny,  Iside S. Parrichini, Tobias M. Gasser,  and Thomas Loerting^{a)} 

AFFILIATIONS

Institute of Physical Chemistry, University of Innsbruck, Innrain 52c, A-6020 Innsbruck, Austria

Note: This paper is part of the JCP Special Topic on Slow Dynamics.

^{a)} Author to whom correspondence should be addressed: thomas.loerting@uibk.ac.at

ABSTRACT

The nature of the hydrogen substructure of a deuterated and deuterium chloride (DCI)-doped ice VI sample after cooling at 1.8 GPa has been a topic of recent interest—especially because the novel ice polymorph ice XIX was discovered in the course of such studies. We here investigate deuterated samples containing 5% H₂O using Raman spectroscopy to probe for transitions associated with rearrangement of D-atoms in ice XIX. The protocol involving heating at subambient pressure (10 mbar) in this study follows closely the one used in our earlier neutron diffraction study. Heating of ice XIX induces a complex cascade of processes involving both ordering and disordering of D atoms. Our Raman spectra demonstrate that the transition sequence is ice XIX → ice VI[‡] → ice XV, in accordance with our earlier neutron diffraction result. First signs for ice XIX decay are evident at 100 K, while ice XV build-up is seen only at 108 K and above. Between 100 and 108 K, a transiently disordered D-substructure appears, where at 108 K, ice VI[‡] forms from ice XIX and simultaneously decays to produce ice XV—thereby establishing a dynamic equilibrium. Using isothermal, time-resolved Raman spectroscopy in real time, we here determine rate constants, Avrami exponents, and activation energies for both slow processes, ice XIX decay and ice XV build-up. The first transition in this sequence, ice XIX decay, is faster than the second transition, ice XV build-up, so that ice VI[‡] accumulates. On the basis of the Johnson–Mehl–Avrami–Kolmogorov data obtained from the isothermal Raman experiment, we additionally report kinetic models for the development of fractions of ices XIX, XV, and VI[‡] in non-isothermal heating experiments at different heating rates. These models consider the two coupled first-order transitions as separated processes, where the phase fractions are calculated for incrementally small temperature (or time) steps. These models compare favorably with our previous observations for slowly or rapidly heated ice XIX samples, such as in calorimetry or neutron diffraction experiments.

© 2022 Author(s). All article content, except where otherwise noted, is licensed under a Creative Commons Attribution (CC BY) license (<http://creativecommons.org/licenses/by/4.0/>). <https://doi.org/10.1063/5.0087592>

INTRODUCTION

Ice XIX is the most recent discovery of ice phases.¹ Its crystal structure was determined based on neutron diffraction experiments on the deuterated isotopologue.² In total, now 20 different ice polymorphs are known—where recently also pure cubic ice I_c could be made in the laboratory.^{3,4} Possible superionic candidates for ice XX have also been reported at ultrahigh-pressure, where the crystal structure elucidated from neutron diffraction measurements is missing so far.⁵ Furthermore, three amorphous ices⁶ add to the complexity of solid H₂O, which is probably the most complex single-component system in chemistry. One reason for this diversity is the occurrence of most ices in pairs, consisting of a hydrogen-disordered

high temperature phase and a hydrogen-ordered low temperature phase, such as ices I_h–XI,^{7,8} III–IX,⁹ V–XIII,¹⁰ VII–VIII,¹¹ and XII–XIV.¹⁰ For ice II, the disordered counterpart is missing still but could be realized as the H₂O-lattice of a hydrogen clathrate hydrate.¹² All of these ice polymorphs feature an oxygen lattice with each oxygen atom being covalently connected to two hydrogen atoms, i.e., the crystals are composed of H₂O molecules. Furthermore, each oxygen atom is connected to four other water molecules through H-bridges—this is known as the Bernal–Fowler ice rules.¹³ Any crystalline ice phase composed of H₂O molecules contains O-atoms on lattice positions, i.e., the O-atoms define a periodically ordered crystal structure. The H-atom configuration, on the other hand, may or may not be periodically

ordered. The former is then termed an H-ordered ice, in which the orientation of water molecules follows a long-range pattern. The latter is termed an H-disordered ice, in which the orientation of each water molecule is random—the water dipoles are disordered. Random in this context more precisely means that the positions of the H-atoms do obey the Bernal–Fowler ice rules, where all of the many possible configurations in accordance with these rules are taken with equal probability. Whereas the H-atoms can switch between different configurations at higher temperatures, their mobility drops at lower temperatures, and they get trapped in one of these random configurations. This is then also referred to as “glassy ice” or “orientational glass” to highlight the randomness. Note that the term “glass(y)” then refers to the subset of H atoms only but not to the (crystalline) O-lattice. That is, the very same lattice and O-atom topology may be shared between different ice polymorphs.

Ice VI is one of the high-pressure, H-disordered polymorphs, which is stable at 0.6–2.2 GPa.¹⁴ In the case of the ice VI lattice of O-atoms, three different crystal structures are now known: disordered ice VI, discovered in 1965;¹⁴ partly ordered ice XV, discovered in 2009;¹⁵ and partly ordered ice XIX, discovered in 2018 by our research group¹ and crystallographically refined by Yamane *et al.*¹⁶ and our group in 2021.² Up until recently, it was believed that all ice phases would occur in pairs, with exceptions of the ultra-high-pressure phases ice X¹⁷ and XVIII,¹⁸ which violate the Bernal–Fowler rules and lack intact H₂O molecules. This idea of ice pairs has been maintained despite some counterparts missing experimental confirmation. Specifically, the disordered counterpart to ice II and the ordered counterpart to ice IV still await their discovery. This dogma changed in 2018 when some of us discovered ice XIX based on thermograms, dielectric loss spectra, Raman spectra, and x-ray diffraction patterns differing from all other ice polymorphs.¹ Ice XIX represents the second hydrogen-ordered proxy of ice VI and features a structure different from its sibling ice XV.² Ice XV,¹⁵ just like ice XIX, is obtained by cooling ice VI under high-pressure conditions. The higher the pressure, the more likely ice XIX will form upon cooling ice VI. At 1.8 GPa, ice XV no longer forms, at 1.0 GPa, ice XV forms predominantly, with some ice XIX as a by-phase, and at 0.0 GPa (ambient pressure), only ice XV but no ice XIX forms upon cooling ice VI.¹⁹ That makes the first case for a trio of distinct ice polymorphs sharing the same network of oxygen atoms. We note that an alternative crystal structure for ice XIX was proposed by Salzmann *et al.*,²⁰ where the ice investigated by them was not made using the protocols known to produce ice XIX. Hence, the crystal structure reported by them may simply be a different kind of ice, and it will not be considered further in this work.²¹

Upon heating at ambient pressure, ice XIX undergoes a transition to ice XV. That transformation represents the first known order-to-order transition of H atoms in ice chemistry. However, the transformation does not take place in a simple one-step process. Our calorimetry measurements suggest that the substructure of H-atoms in ice XIX initially disorders before it reorders to attain the ice XV structure.¹⁹ In the temperature interval between the initial disordering of ice XIX and the final ordering to ice XV, at least two processes take place simultaneously. Most features characteristic for the H-order of either ice XV or ice XIX are absent in that temperature range, which was identified to be between 100 and 115 K in our neutron-diffraction² and earlier Raman spectroscopy experiments.²² In this temperature interval, we found Bragg peaks and

spectral features that are typical for ice VI. Accordingly, the transformation from ice XIX to XV passes through a hydrogen-disordered transition state called ice VI[‡].² Such behavior can also be rationalized upon inspection of the crystal structures: in order to convert ice XIX to ice XV, the occupancies of almost all H-sites need to be changed, where the path from one to the other necessarily needs to pass through a disordered state. The occurrence of such a transition state means that kinetics is of key importance, where different time scales in different experiments lead to more or less formation of ice VI[‡] in the temperature interval between 100 and 120 K. The transition is quite slow and takes place on the time scale of minutes, hours, or even days in this interval.

The phase mixtures appearing in this temperature interval have so far only been identified qualitatively in our earlier calorimetry¹⁹ and neutron diffraction experiments, though.² A quantitative elucidation of the slow reaction kinetics for this order-to-order transition has remained elusive so far and, thus, represents the primary aim here. In the present work, we follow both the kinetics of ice XIX decay and the kinetics of ice XV build-up on the basis of Raman experiments in real time. Neutron diffraction would be another technique suitable for this task in the case of deuterated ice XIX. We here decide for Raman spectroscopy because this technique can also be employed to study the H-atom kinetics of hydrogenated ices, in contrast to neutron diffraction. We will report the H-atom kinetics in ice XIX/XV/VI in a follow-up work and extract the isotope effect on the kinetics from this comparison directly. The choice of reporting the data on the deuterated form in the present paper first allows us to compare the results to our earlier heating experiments done in the neutron diffraction instrument. In our earlier work on Raman spectroscopy of ice XIX, we have reported spectra for protiated ice XIX, and so the secondary goal of this work is to show the isotope effect on the Raman spectra in the ice VI/XV/XIX trio. The primary kinetics task has turned out to be challenging as the structures of ice VI, XV, and XIX are very similar to each other. The key problem to unravel the reaction kinetics is that a method needs to be able to simultaneously quantify the relative fractions of ice VI, XV, and XIX in a single experiment. It has not been possible to obtain this information from methods such as x-ray or neutron diffraction or calorimetry so far. Calorimetry, for instance, is blind to ice VI.¹⁹ X-ray diffraction shows only very subtle differences between the three ices, since the diffracted intensity mainly stems from the electrons surrounding the oxygen atoms. Neutron diffraction does not allow us to quantify relative fractions of all the three, even though Bragg peaks can be identified that are characteristic of ices VI, XV, or XIX. In addition, in Raman spectroscopy, which we employ here as the key method, the task of real-time experiments is highly challenging. Most notably quantification of polymorph fractions is hampered by small cross sections of bands, but still it turns out to be the most suitable method. Raman spectroscopy provides a set of relatively well-resolved bands for ice XV, XIX, and VI/VI[‡] and offers, thereby, a possibility to identify fractions of each individual phase and to monitor ice XIX decay and ice XV build-up even if they take place simultaneously. In order to obtain a sufficient signal-to-noise ratio, we here have to accumulate for about 3 min/spectrum, which represents the limiting factor in terms of time resolution. That is, we here follow the slow transformation kinetics taking place on the time scale of minutes and hours in real time. Fractions of ice XIX, XV, and VI[‡] are determined for every single spectrum

through superposition of the spectra of pure ice VI and XV and initial ice XIX, recorded at each respective temperature. In this context, “pure” refers to the absence of other ice phases that show a different space group, i.e., the absence of other ices with other Roman numbers. “Pure” does not imply full hydrogen order, though. Both ice XIX and ice XV are partly hydrogen-ordered ice phases. Rate constants are derived from isothermal experiments based on a modified Johnson–Mehl–Avrami–Kolmogorov (JMAK) plot²³ (see the section titled Experimental Section). Isothermal experiments at different temperatures allow us to simultaneously extract activation energies both for the ice XIX decay (to ice VI[‡]) and the ice XV build-up (from ice VI[‡]) based on Arrhenius plots from the rate constant data. Ultimately, we use the kinetic data obtained here to parameterize a kinetic model that allows us to calculate the ice polymorph fractions in slow and in fast heating experiments of ice XIX. This, in turn, allows us to better understand the different phase fractions observed in experiments for widely varying heating rates ranging from less than 1 K h⁻¹ to 100 K min⁻¹.

EXPERIMENTAL SECTION

Ice XIX samples containing 95% D₂O and 5% H₂O were prepared exactly as outlined in Ref. 2. In short, 95 wt. % of D₂O were mixed with 5 wt. % of H₂O in the liquid state. Rapid exchange then leads to the formation of almost 10% HDO and a minor number of H₂O molecules. The solution was then acidified using 0.01M deuterium chloride (DCl) in D₂O, which leads to introduction of point defect into the ice lattice upon freezing. Hexagonal ice is converted to ice VI through compression in a piston-cylinder setup at 77 K and isobaric heating to 255 K, typically at 1.8 GPa and 1–2 K min⁻¹ heating rate. DCl-doped ice VI is then cooled at 1.8 GPa, initially at 3 K min⁻¹ to 150 K, and then even more slowly (0.5 K min⁻¹) to 90 K to produce deuterated ice XIX. The ice XIX sample containing 95% H₂O and 5% D₂O was prepared analogously to Ref. 1 with the isotopic mixture being doped with 0.01M HCl and the sample being cooled down from 255 to 90 K with 3 K min⁻¹ at 1.8 GPa.

Ice XV samples were prepared as outlined by Shephard and Salzmann.²⁴ That means 0.01M DCl-doped ice VI was quenched at 1.0 GPa at ≈40 K min⁻¹ to 80 K. The samples were then recovered from the pressurized steel cylinder to ambient pressure and stored in liquid nitrogen. Upon release of pressure at 77 K, the topology and degree of (dis)order do not change, as demonstrated in our earlier work on ice VI/XV/XIX.^{1,2,19} However, upon heating ice XV at ambient pressure and recoiling to liquid nitrogen temperature, the degree of order in ice XV is enhanced. This cooling was done from 133 to 84 K at a rate of about 1 K min⁻¹ directly within the Raman cryostat. As demonstrated in our earlier work, this procedure removes unwanted ice XIX contamination from ice XV.¹⁹ The ice VI reference is prepared at 1.0 GPa by rapidly quenching undoped D₂O ice VI at ≈65 K min⁻¹.

After recovery of the ice XIX (or ice XV) samples from the high-pressure cylinder to ambient pressure, the samples were stored in liquid nitrogen and handled while permanently immersed in nitrogen. For Raman measurements, small grains of the powdered ice were transferred to the Raman cryostat (Oxford N Microstat), which was precooled to 84 K and coupled to the microscope. Raman spectra were taken using a confocal WITec alpha300 R Raman microscope, including a laser of a wavelength of 532 nm

and maximal power output of 20 mW with a ZEISS LD Plan-NEOFLUAR/40×-objective. During the measurement, the cryostat was evacuated to 10 mbar. Temperature was controlled by a Lakeshore 331S temperature controller. The laser power was adjusted to avoid degradation of the spectra through unwanted sample heating. For each spectrum, the integration time was set to 3–10 min, depending on the signal/noise ratio at the spot of measurement, which is about 1 μm in diameter. The spectra were collected using a 600 grooves/mm grating and a CCD-camera.

The development of each of the phases was scrutinized through the continuous recording of Raman spectra during isothermal heating experiments at different temperatures. As shown in Fig. S1 in the [supplementary material](#), the phase composition at each specific point was determined through superpositions that were performed analogously to those shown in our earlier publication.²⁰ For this reason, ice XV- and ice VI-spectra recorded at the same temperature were employed as reference. The first spectrum of the respective temperature series was utilized as ice XIX-reference. Rather than attempting a superposition of three ice phases at once, we analyzed superpositions of the ice XIX and ice VI pair, on the one hand, and of ice VI and ice XV, on the other hand, independently. Choosing the spectral range was quite challenging. As the coupled OD-stretching bands show the highest intensities and provide well-resolved characteristic signals for each of the three phases, they seem to be the obvious choice on the first glance. The ambiguous baseline in that range causes a significant systematic error. Therefore, the most suitable spectral range for the former superposition is the decoupled OH-stretching range and librational band for the latter (see Fig. 1 and the section titled Results for more details).

The superposition analysis provides us with the change of phase fractions with time under isothermal conditions. These isotherms are fitted by the modified JMAK-equation²³ both for ice XIX decay and for ice XV build-up, as shown in Eqs. (1a) and (1b). For that matter, the initial ice XV-fraction after reaching a given temperature was set to 0 in order to consider the changes of the ice XV-fraction developed under isothermal conditions exclusively. This fitting procedure provides us with rate constants k^{XIX} and k^{XV} as well as Avrami exponents n^{XIX} and n^{XV} at several different specific temperatures,

$$f(\text{XIX}) = e^{-(k^{\text{XIX}}t)^{n^{\text{XIX}}}}, \quad (1a)$$

$$f(\text{XV}) = 1 - e^{-(k^{\text{XV}}t)^{n^{\text{XV}}}}. \quad (1b)$$

In order to model phase fractions not only in isothermal waiting experiments but also in heating experiments, we need to take into account the temperature dependence of the rate constants and Avrami exponents. The temperature dependence of rate constants is obtained through an Arrhenius fit as given in Eq. (2), where E_A represents the activation energy for the phase transformation and A is a pre-factor,

$$k = A \cdot e^{-\frac{E_A}{RT}}. \quad (2)$$

Strictly speaking, the Avrami equation is valid for a first-order phase transition $A \rightarrow B$ under isothermal conditions only. In our attempt of modeling phase fractions in slow and fast heating experiments, we need to know the Avrami equation for many different temperatures. In our experiment, we are not only speaking about the reaction

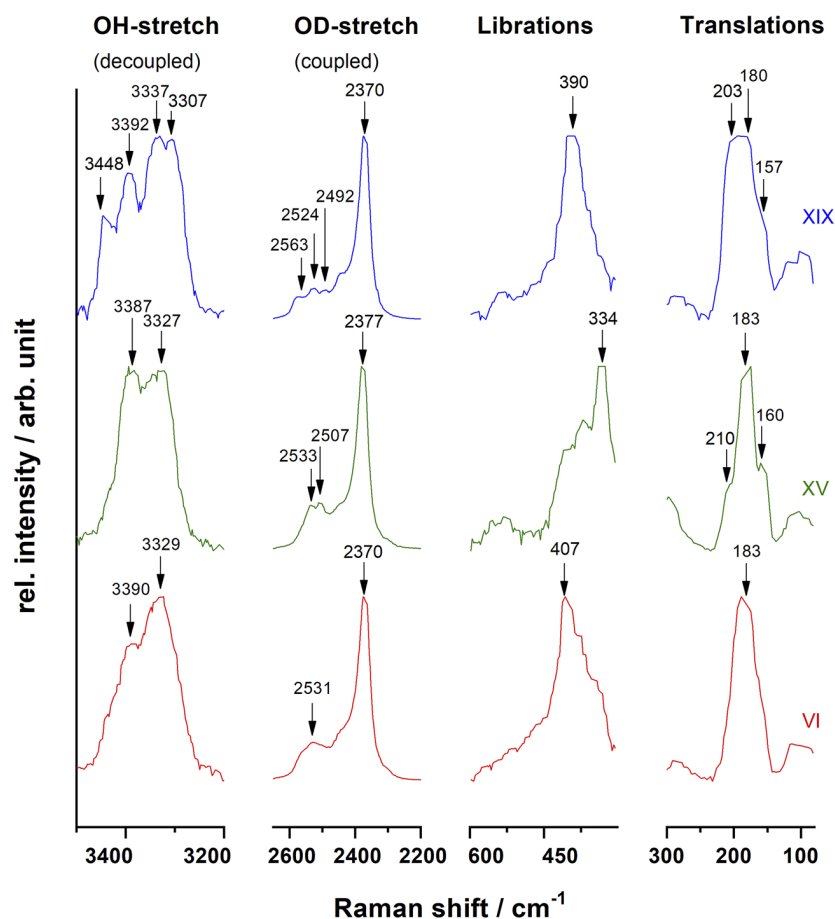


FIG. 1. Raman spectra of deuterated ices VI, XV, and XIX (containing 5% H₂O) at 84 K. Spectra were normalized for matching intensities of the most intense band in each range.

A → B but also about the coupled process, A → B → C, i.e., ice XIX → ice VI[‡] → XV. To model the kinetics, we have decided to derive the Avrami equation individually for A → B and B → C at several temperatures. In order to model phase fractions upon heating, we use a step-by-step iterative equation that relies on interpolated Avrami parameters both for ice XIX → ice VI[‡] and ice VI[‡] → XV. Apparently, the Avrami parameters are not independent from each other, and the parameters change as more and more ice VI[‡] builds up. This change reflects underlying physics, such as different types of growth and the presence of more domain boundaries. The development of the Avrami exponents with temperature is not reflected in any theory, though, and so we have empirically estimated its temperature dependence and assumed three different variants for modeling phase fractions in heating experiments. That is, rather than learning much about the underlying physics, we here use an empirical approach where the parameters do not rigorously take into account how much ice VI[‡] is present. There is certainly a better separation between the two individual processes for slow heating experiments so that the approach of separating the whole process into two individual contributions is justified better than for fast heating experiment. In order to determine the development of the fraction of all three phases during heating at different heating rates, we use these three different kinetic models on the basis of the JMAK fits to the isothermal development of fractions with time. We

do this in the present work using an iterative process, where ice fractions are calculated for every single step on the basis of the previous step, where a step is defined through a small change in temperature. A change in temperature is equivalent to a change in time, given a specific heating rate. The temperature ramp in the heating experiment is approximated through a step-wise isothermal processes of 1K-intervals (“saw pattern”). As starting point, ice XIX at 100 K was utilized, i.e., $f(\text{XIX}, 100 \text{ K}) = 1.0$. Its decay during the heating process is then described through

$$f(\text{XIX})_i = f(\text{XIX})_{i-1} \cdot e^{-(\Delta t \cdot k(T)_i^{\text{XIX}})^{n_i^{\text{XIX}}}}. \quad (3)$$

In this iterative equation, the index $i - 1$ represents the previous step, i represents the current step, and Δt represents the time between two steps. In other words, $f(\text{XIX})_{100\text{K}}$ represents the ice XIX fraction at 100 K, and $f(\text{XIX})_{101\text{K}}$ represents the fraction at 101 K. It is determined through the amount of ice XIX that has decayed in the time it takes to heat by 1 K. For different heating rates, the same temperature step ΔT corresponds to a different time step Δt . For the determination of the development of the ice XV-fraction $f(\text{XIV})$, on the other hand, the fraction of its mother phase, ice VI[‡], at the previous step has to be taken into account, as shown in the following equation:

$$f(\text{XV})_i = f(\text{XV})_{i-1} + \left(1 - f(\text{XIX})_{i-1} \cdot e^{-(\Delta t \cdot k(T)_i^{\text{XIX}})^{n_i^{\text{XIX}}}}\right) \cdot f(\text{VI}^\ddagger)_{i-1} \cdot e^{-(\Delta t \cdot k(T)_i^{\text{XV}})^{n_i^{\text{XV}}}} \quad (4)$$

The ice VI[‡]-fraction is represented by the remainder,

$$f(\text{VI}^\ddagger)_i = 1 - f(\text{XIX})_i - f(\text{XV})_i \quad (5)$$

The three models differ from each other in terms of their Avrami exponents, especially on how these parameters change with temperature. That is, model 1 sketches the temperature development as directly obtained from our Raman experiment and summarized in Table II. Model 2 applies temperature independent average values. In addition, model 3 uses temperature independent values for n , where we attempted many combinations of exponents and use the ones for model 3 that qualitatively match the experimental observations best. Our criterion for best match is which phase appears or disappears at which temperature for different heating ramps. For instance, barely any ice XV forms in fast calorimetry heating scans for deuterated ice XIX, and the temperature at which ice XIX

TABLE I. Raman band positions for 95% deuterated ice XIX (from Fig. 1 here, second column) in comparison with 95% protiated ice XIX, both at 84 K. The values in the first column were measured using a 600 grooves/mm grating, which deviate by no more than 3 cm⁻¹ from the values reported by us earlier in Ref. 22, Fig. 2 measured using a 1800 grooves/mm grating. The isotope effect is given in the third column, where the values are calculated as the ratio between the first and second column, except for the ratios for decoupled bands marked by asterisks (*), which are calculated as the ratio between the second and first column. The Raman spectra for 95% protiated ice XIX used to determine the band positions in the left column are shown in Fig. S3 in the supplementary material.

Ice XIX			Type of bands
$\nu(\text{H}_2\text{O})/\text{cm}^{-1}$ (this work)	$\nu(\text{D}_2\text{O})/\text{cm}^{-1}$ (this work)	$\nu(\text{H}_2\text{O})/\nu(\text{D}_2\text{O})$	
92	96	0.958	Translations
119	114	1.044	
132			
159	157	1.032	
184	180	1.022	
217	203	1.069	
291	277	1.051	
306	291	1.052	Libration
510	390	1.308	
3209	2370	1.354	
3337	2449	1.339	Coupled O-(H,D)-stretching vibration
	2524		
3464	2563	1.344	Decoupled O-(D,H)-stretching vibration
2447	3307	1.352*	
2478	3337	1.345*	
2509	3392	1.352*	
2544	3448	1.344*	

disappears is significantly higher for fast heating than for slow heating experiments. The Raman experiment itself used here can be regarded as a “slow heating” experiment, so the kinetic parameters obtained here are directly suitable for slow heating experiments. It remains unclear whether the same kinetic parameters apply also for fast heating experiments, e.g., a change of mechanism, such as domain growth vs bulk growth, could result from the change of heating rate. Because of this shortcoming, we employ three different kinetic models here. Obviously, a set of experiments aimed at determining kinetic parameters also in the limit of fast heating would be desirable. We lack a fast method to analyze polymorph fractions of ice polymorphs sharing the same oxygen lattice, though. In order to be able to directly compare our data obtained here on deuterated ice samples, we also report a new set of Raman spectra for hydrogenated ice XIX using the same measurement parameters as in the present study (see Fig. S3 in the supplementary material and Table I). Raman spectra for hydrogenated ice XIX measured, e.g., using different gratings, accumulation times, and temperatures, were shown in our previous work on ice XIX.^{1,22}

RESULTS

Raman spectra of deuterated ice XIX

In the present work, we need to establish how to distinguish ices XIX, XV, and VI based on Raman spectra for deuterated samples (containing a small amount of H₂O). To achieve this task, we first need to settle what the Raman spectrum of D₂O ice XIX is. While ice XIX Raman spectra for protiated samples were reported earlier by us, spectra for deuterated ice XIX were missing. In particular, the decoupled OH-stretching band in deuterated ice XIX has not been reported so far. By contrast, Raman spectra of deuterated samples of ice XV and ice VI are available.²² Highly ordered deuterated ice XIX has never been made so far because the ordering kinetics of a fully deuterated sample has proven to be too slow to be accessible on the time scale of several days in our experiments. We merely managed to report librational bands for a weakly ordered deuterated ice XIX in our previous work.²² In the present work, we report Raman spectra of highly ordered 95% deuterated ice XIX for the first time. In principle, in this kind of isotope mixtures, isolated O-H moieties are found in a bath of D₂O molecules—and this allows for the observation of both the coupled OD- and the decoupled OH-stretching vibrations spectroscopically. The decoupling leads to sharper Raman bands, which is very useful for the task at hand involving superposition of spectra to determine relative fractions. In addition to the decoupling also hydrogen-order and hydrogen-disorder have an impact on the width of the band, where more highly ordered domains feature sharper bands. Specifically, in the case of ice XIX, however, the addition of small amounts of H₂O is also important for a different reason: the presence of more mobile protons massively accelerates the deuteron ordering kinetics (see Ref. 1).

Figure 1 shows the Raman spectra for deuterated ice XIX, XV, and VI, where band positions extracted from Fig. 1 are listed in Table I. For ice XV, we have re-cooled an ice VI sample from 135 K at ambient pressure to avoid unwanted ice XIX impurities from the sample.¹⁹ This is especially important because we need the spectra of each individual component as reference spectra for the

superposition procedure to analyze mixed ice VI/XV/XIX spectra. The spectra for deuterated ice XV and ice VI are in excellent agreement with the Raman data reported by Whale *et al.*²⁵ We report the exact same Raman patterns, where wavenumbers agree to within 2 cm^{-1} for the sharp bands and within 6 cm^{-1} for the broader features. In the spectral region of translational bands, we find a relatively broad band centered near 200 cm^{-1} . This band is featureless for ice VI but shows some more structure for ices XV and XIX, e.g., a shoulder at 210 cm^{-1} for ice XV. However, by contrast to the protiated ices (see Fig. 2 in Ref. 22), no well-resolved bands are seen for deuterated ices XV and XIX. Table I also summarizes the isotope effect compared to protiated ice XIX. The characteristic decoupled OH-stretching band for ice XIX is found at 3448 cm^{-1} in Fig. 1. Compared with the decoupled OD-stretching band, this corresponds to an isotope ratio of 1.34, which is close to the typical ratio of $\sqrt{2} = 1.41$ for OH/OD-stretches.²⁶ Similarly, isotopic ratios of 1.34–1.36 are observed for all OD- and OH-stretching vibrations between 2370 and 3450 cm^{-1} . The librational band at 390 cm^{-1}

features a slightly smaller ratio of 1.31, which demonstrates that the libration involves mainly intramolecular OD-motions. By contrast, all translational bands between 100 and 290 cm^{-1} highlight a ratio near 1.05, very close to $\sqrt{20/18} = 1.05$. This indicates that these vibrations are intermolecular in nature, involving all atoms at the same time. Deuterated ice XIX features four well resolved bands, whereas ice XV features only two well resolved bands, and ice VI shows a single band with a shoulder. As for the librational band, we have already identified the specific positions for fully deuterated ice XIX, XV, and VI in our earlier work at 84 K, namely, 380 , 338 , and 402 cm^{-1} (from Table I in Ref. 22). In the present work on 95% deuterated ices, we identify these bands at 390 , 334 , and 407 cm^{-1} , respectively, also at 84 K. For comparison, Whale *et al.* reported the ice VI librational band at 406 cm^{-1} at 80 K.²⁵ The shift between these values may be related to the presence of 5% H_2O in the present work, which is probably the case for ice XIX—where fully deuterated ice XIX samples are only very weakly ordered, but samples containing 5% H_2O much more ordered.² The higher degree of order is then at

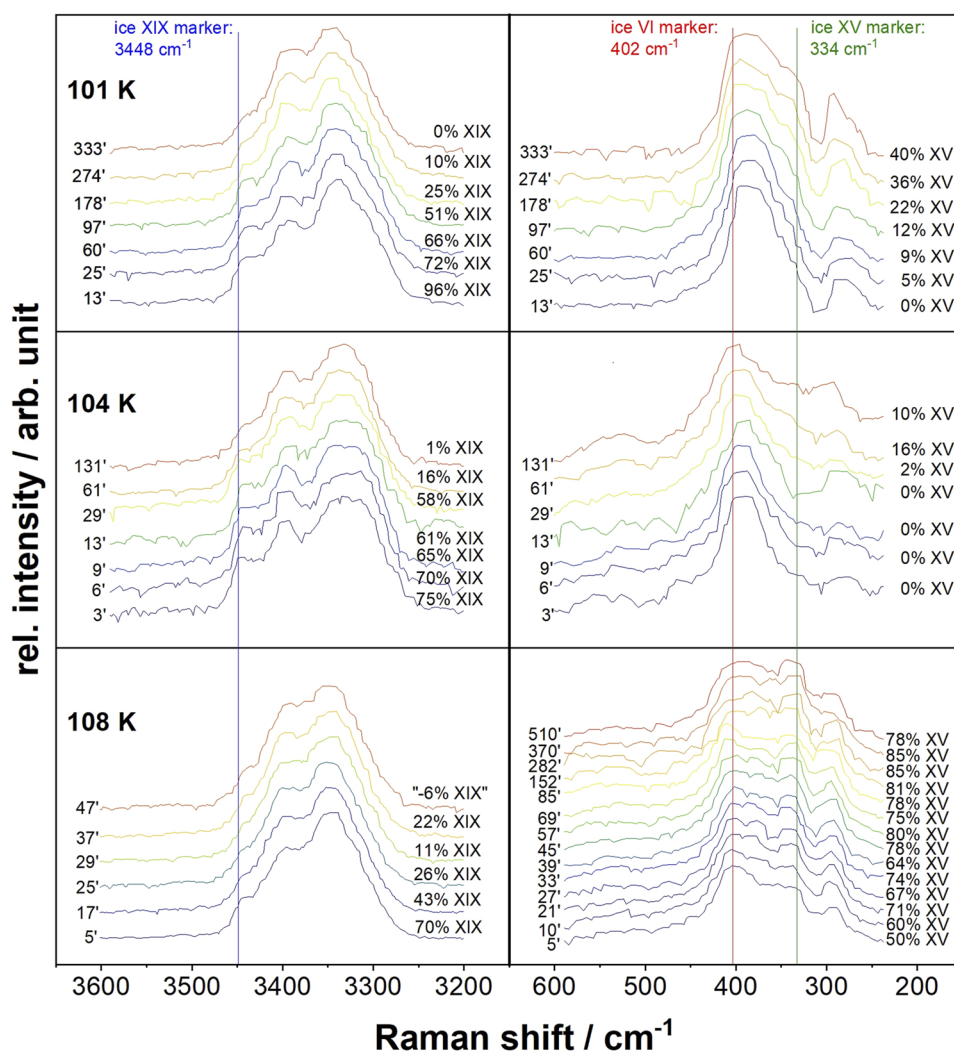


FIG. 2. Ice XIX decay and ice XV build-up at 101, 104, and 108 K. (Left) Decoupled Raman-OH stretching bands for the tracking of the ice XIX \rightarrow ice VI ‡ transition. (Right) Raman librational bands for the tracking of the ice VI ‡ \rightarrow ice XV transition. Vertical lines denote marker bands for ices XIX, XV, and VI, as indicated. Each spectrum is marked with the time passed in the isothermal experiment as well as the result of the superposition analysis. We estimate the error-bar for phase fractions to be $\pm 5\%$.

the origin of the significant blueshift from 380 to 390 cm^{-1} . In addition, the bands also shift with temperature changes. In particular, in the case of ice VI, there is a pronounced redshift of this band from 407 to 402 cm^{-1} upon heating to 100 K.

Raman spectroscopic distinction of deuterated ices XIX, XV, and VI

In our recent Raman work, we have identified marker bands to distinguish ice VI, ice XV, and ice XIX.²² For hydrogenated samples, we have employed the intensity ratio of the bands at 220 and 160 cm^{-1} , also known as the Whale index,²⁵ to measure the degree of H-order, where the index decreases from 0.33 ± 0.02 in ice XIX to 0.18 ± 0.02 in ice XV and 0.00 in ice VI. However, the Whale index cannot be defined unambiguously in the deuterated case and, of course, is also unsuitable for the real-time observation of kinetics. The reason is that the characteristic signal is separated from the band at $\sim 180 \text{ cm}^{-1}$ for protiated samples but merges with the latter in spectra of deuterated ones due to the isotope effect. By contrast, the OH/OD-stretching bands as well as the librations clearly allow distinction between ices VI, XV, and XIX. For protiated ices, we have defined the decoupled OD-index as the intensity ratio of the band maximum at 2542 cm^{-1} compared to the minimum at 2530 cm^{-1} . This index is well suitable to distinguish ice XIX from ice XV and ice VI, but it is not suitable to distinguish ice XV and ice VI. Specifically, the OD-index for hydrogenated ice XIX is 1.30 ± 0.10 and about 0.60–0.70 for both ice XV and ice VI. In order to also distinguish ice XV from ice VI, we have looked at the librational index, defined as the ratio of the intensity at 450 cm^{-1} to the integrated intensity at 450 and 510 cm^{-1} . The librational index is 0.90 ± 0.05 for ice XV and 0.20–0.30 for both ice XIX and ice VI. That is, the bands at 450 and 2542 cm^{-1} are characteristic for ice XV and ice XIX, respectively. Compared to the translational bands, the librational bands are well resolved against each other. The decoupled OD-stretching band is quite sharp and has a significant cross section, despite only some HOD molecules in a bath of H_2O molecules.

The decoupled OH-stretching band clearly distinguishes ice XIX from ice VI and ice XV. That is, the characteristic feature of deuterated ice XIX at 3448 cm^{-1} allows an unambiguous distinction from ices XV/VI, and the librational bands at 334 and 402 cm^{-1} allow unambiguous identification and quantification of ices XV and VI, respectively. These three marker bands are, therefore, used in our superposition analysis in the isothermal, real time experiments shown in Fig. 2.

Ice XIX decay at 101–108 K

When heating ice XIX from liquid nitrogen temperature (77 K), it starts to disappear slightly above 100 K. The calorimetric onset temperature for deuterated ice XIX was determined to be $106 \pm 1 \text{ K}$ using a heating rate of 10 K min^{-1} .² This is about 3 K higher than the onset temperature for protiated ice XIX.^{1,19} In the much slower heating experiments in the cryostat at the HRPD-neutron diffraction instrument, first signs for the disappearance of the characteristic ice XIX Bragg peak at 1.87 Å are evident at 100 K, and at 105 K, deuterated ice XIX has fully disappeared (see Fig. 3 in Ref. 2). In the present work, the time spent isothermally at each temperature

is about 400–500 min, and the heating rates are about 4 K min^{-1} . This is close to the time scales in the neutron experiment—that is, we expect first signs of disappearance already at 100 K. Figure 2 reports exemplary sequences of spectra for the isothermal Raman experiments at 101, 104, and 108 K, accumulating spectra every 3 min. Additional raw Raman data for the isothermal waiting experiments at higher temperatures are shown in the supplementary material (Fig. S2). In the Raman experiment reported here, we are unable to detect disappearance (or change of spectra) at 98 K even after 5 h. By contrast, the ice XIX marker band at 3448 cm^{-1} vanishes with time at 101–108 K in Fig. 2 (see left column). In the moment that the temperature is reached (at 0 min), already a small fraction of ice XIX has vanished during the heating process prior to the isothermal measurements. For example, at 104 K, the fraction of ice XIX shrinks from 75% to 65% in the first 9 min of measurement. After 131 min, basically no ice XIX is left at 104 K (see Fig. 2). At 101 K, we do see significant disappearance of deuterated ice XIX after one hour, and full disappearance after six hours. This is also indicated in the black curve in Fig. 3(a), which summarizes the fraction of ice XIX remaining as a function of time at 101, 104, and 108 K from Fig. 2. At 104 and 108 K, full disappearance is reached after about two and one hours, respectively. The three marker bands for ices VI, XV, and XIX used to extract the data for Fig. 3(a) are highlighted using dashed vertical lines for the isothermal experiments in Fig. 2. Contrary to the observations at 104 K and below, the ice XV marker band at 334 cm^{-1} grows with time at 108 K, while the ice VI marker band at 402 cm^{-1} essentially remains stable. At 108 K, ice XIX disappears entirely within less than one hour. At higher temperatures, we

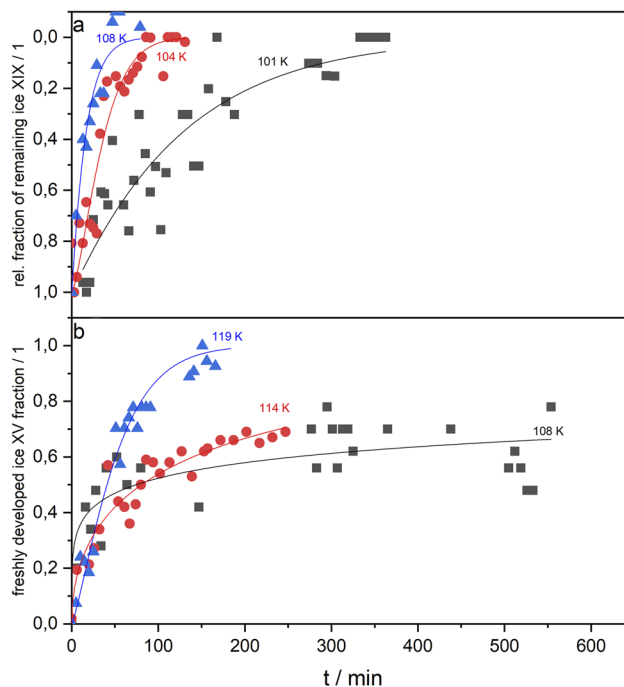


FIG. 3. Time evolution of (a) ice XIX \rightarrow ice VI[‡] and (b) ice VI[‡] \rightarrow ice XV. We estimate the error-bar for phase fractions to be $\pm 5\%$.

are unable to follow the rapid disappearance systematically because our Raman accumulation time of three minutes at best is too slow for a collection of a sufficient amount of points.

Ice XV build-up at 108–119 K

At 108 K, we actually do see the disappearance of ice XIX in the decoupled OH-stretching band region simultaneously with the appearance of ice XV, which we monitor in the librational band region. In Fig. 2, we clearly see how the band at 334 cm^{-1} grows with time. Interestingly, the marker band for ice VI^{\ddagger} at 402 cm^{-1} stays roughly constant at the same time. However, note that the ice XIX marker band is very close, at 390 cm^{-1} , so that it is difficult to disentangle ice XIX and ice VI^{\ddagger} in the librational band range alone. This is only possible when simultaneously inspecting the ice XIX marker band at 3448 cm^{-1} as done in Fig. 2. This means that ice VI^{\ddagger} is not depleted at 108 K—a finding that we interpret as a dynamic equilibrium for ice VI^{\ddagger} . In this dynamic equilibrium, the ice VI^{\ddagger} fraction transforming to yield ice XV is replenished by ice XIX decaying to ice VI^{\ddagger} . In other words, on the one hand, it is continuously formed through ice XIX disappearance, and on the other hand, it is continuously disappearing because of its transformation to ice XV. The net effect at 108 K is transformation from ice XIX to ice XV, but we clearly see the transient state to persist for hours. The equivalence of the transiently appearing band with the ice VI band shows that the transformation from ordered ice XIX to ordered ice XV takes place via a disordered transition state. Below 108 K, we are able to detect disappearance of ice XIX but hardly any growth of ice XV. At 108 K, we observe both processes at the same time, and above 108 K, we only see growth of ice XV. The temperature of 108 K allows us to directly compare the time scales: ice XIX has fully disappeared after one hour, but ice XV grows for many hours at 108 K. That is, ice XIX disappearance is the faster process. At 114 and 119 K, the build-up of ice XV is significantly faster. It is complete after two hours at 119 K, whereas it has only reached $\sim 60\%$ after nine hours at 108 K (see Fig. S2 in the supplementary material).

Fitting of JMAK kinetics for both slow transformations

Figure 2 also indicates the fractions of ice XIX (left column) and ice XV (right column) determined from the spectral superposition procedure. In Fig. 2 ice XV starts at 0% for 101 and 104 K, but already at about 50% at 108 K, and then grows to about 85% in the course of a few hours. Note that the uncertainty in the fractions of ice XV maybe up to $\pm 10\%$, which is due to the noise in each single spectrum and the broadness of the marker band collected for only 3 min. The sharper marker band for ice XIX and its larger cross section allow for better signal-to-noise ratio and smaller error-bars of about $\pm 5\%$ for fractions determined from the superposition procedure. Figure 3 collects all data points for several temperatures, where the top panel shows ice XIX disappearance and the bottom panel shows ice XV appearance. These data are employed to extract parameters for the kinetic model. Quantitatively the rate constants are obtained through a modified JMAK-fit to the data by using Eq. (1), where both the rate constant k and the Avrami exponent n are fit parameters. The best fit parameters are listed in Table II. The Avrami exponent n is consistently close to 1 for ice XIX disappearance and grows from

TABLE II. Rate constants k and Avrami exponents n for the two slow processes, ice $\text{XIX} \rightarrow \text{VI}^{\ddagger}$ and ice $\text{VI}^{\ddagger} \rightarrow \text{XV}$. Values are determined based on the fits shown in Fig. 2.

	$k_{\text{XIX} \rightarrow \text{VI}^{\ddagger}}/\text{min}^{-1}$	$n_{\text{XIX} \rightarrow \text{VI}^{\ddagger}}/1$	$k_{\text{VI}^{\ddagger} \rightarrow \text{XV}}/\text{min}^{-1}$	$n_{\text{VI}^{\ddagger} \rightarrow \text{XV}}/1$
101 K	0.0089	0.84		
104 K	0.0258	1.40		
108 K	0.0594	1.05	0.0026	0.22
114 K			0.0060	0.51
116 K			0.0059	0.64
119 K			0.0157	0.89

0.22 to almost 1 for ice XV build-up between 108 and 119 K. The reason for the very low exponent at 108 K is presumably that ice XV build-up is hampered by the lack of ice VI^{\ddagger} . Ice VI^{\ddagger} is delivered only slowly through ice XIX decay, and hence, ice XV build-up is stretched to longer times. The higher the temperature, the more readily is ice VI^{\ddagger} available, and ice XV growth proceeds faster and faster. At 119 K, the Avrami exponent for ice XV build-up is very similar to the Avrami exponent for ice XIX decay at 101 K. The rate constants k grow by a factor of 6 for ice XIX decay from 101 to 108 K and also by a factor of 6 for ice XV build-up from 108 to 119 K. At 108 K, ice XIX decay is about 25 times faster than ice XV build-up.

The rate constants extracted from Fig. 3 are plotted in Arrhenius form in Fig. 4 based on the Arrhenius equation given in Eq. (2). According to the Arrhenius fit in Fig. 4, the activation energy for ice XIX decay is about 24 kJ mol^{-1} . This is smaller than the activation energy for dielectric relaxation of 45 kJ mol^{-1} in our earlier work.¹ The rate constants for ice XV build-up also grow with increasing temperature. However, also the Avrami exponent n grows with temperature. This means that the activation energy of 18 kJ mol^{-1} for

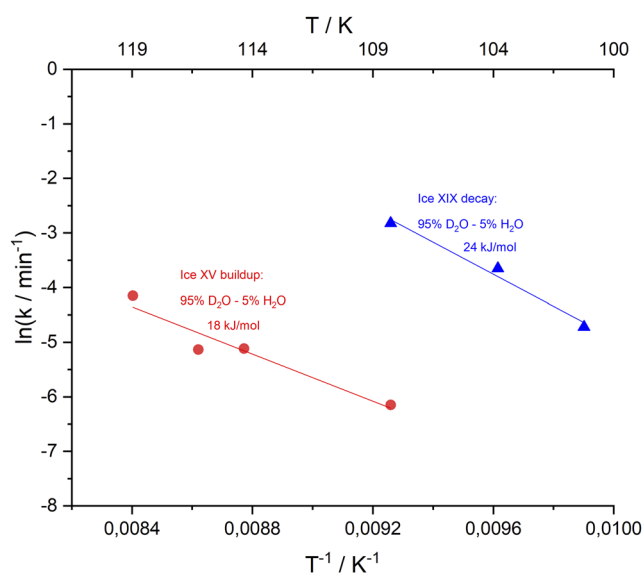


FIG. 4. Arrhenius plot for ice XIX decay (triangles, blue line) and ice XV build-up (circles, red line). Rate constants are given in units of min^{-1} .

ice XV build-up is an apparent activation energy that is affected by the amount of ice VI[‡] that is delivered from ice XIX decay. This finding also explains our earlier result on activation energies for dielectric relaxation of ice XV: in a fully developed ice XV sample, we had found an activation energy of 27 kJ mol⁻¹;¹ in an ice XV that was produced in real time from ice XIX, the activation energy was only 18 kJ mol⁻¹. This implies that the activation energy for dielectric relaxation of ice XV is lowered by the presence of transient ice VI[‡].

Modeling fractions of ice XIX/XV/VI[‡] in heating experiments

Finally, we try to calculate the fractions of ice XIX, ice VI[‡], and ice XV as a function of temperature in heating experiments based on the kinetic data reported in Fig. 4 and Table II. To this end, we use the iterative equations (3)–(5). This aims at understanding the findings in our previous heating experiments of ice XIX, especially

calorimetry and neutron diffraction scans. Since these experiments differ widely in terms of heating rates, Fig. 5 shows models for three different heating rates close to the ones employed in our earlier experiments, namely, 1 K h⁻¹, 1 K min⁻¹, and 30 K min⁻¹. As mentioned in the section titled Experimental Section, there is no rigorous way of defining the parameters in the coupled process that contains two first-order transitions and involves three different types of ices. Most notably, all parameters will be influenced by the presence of more or less of the transient state, ice VI[‡]. In the models, we employ three different empirical strategies regarding the temperature dependence of the Avrami exponents: in the first set, Avrami exponents change with temperature, similar to the values listed in Table II. Using this set, the build-up of ice XV at 1 K h⁻¹ is way faster than what we observe. Already at 105 K, ice XV build-up is complete. In the second set, we employ temperature independent Avrami exponents representing an average of the values in Table II. This model fails especially for faster heating rates, in which ice XIX persists to much higher temperatures than in experiment, whereas

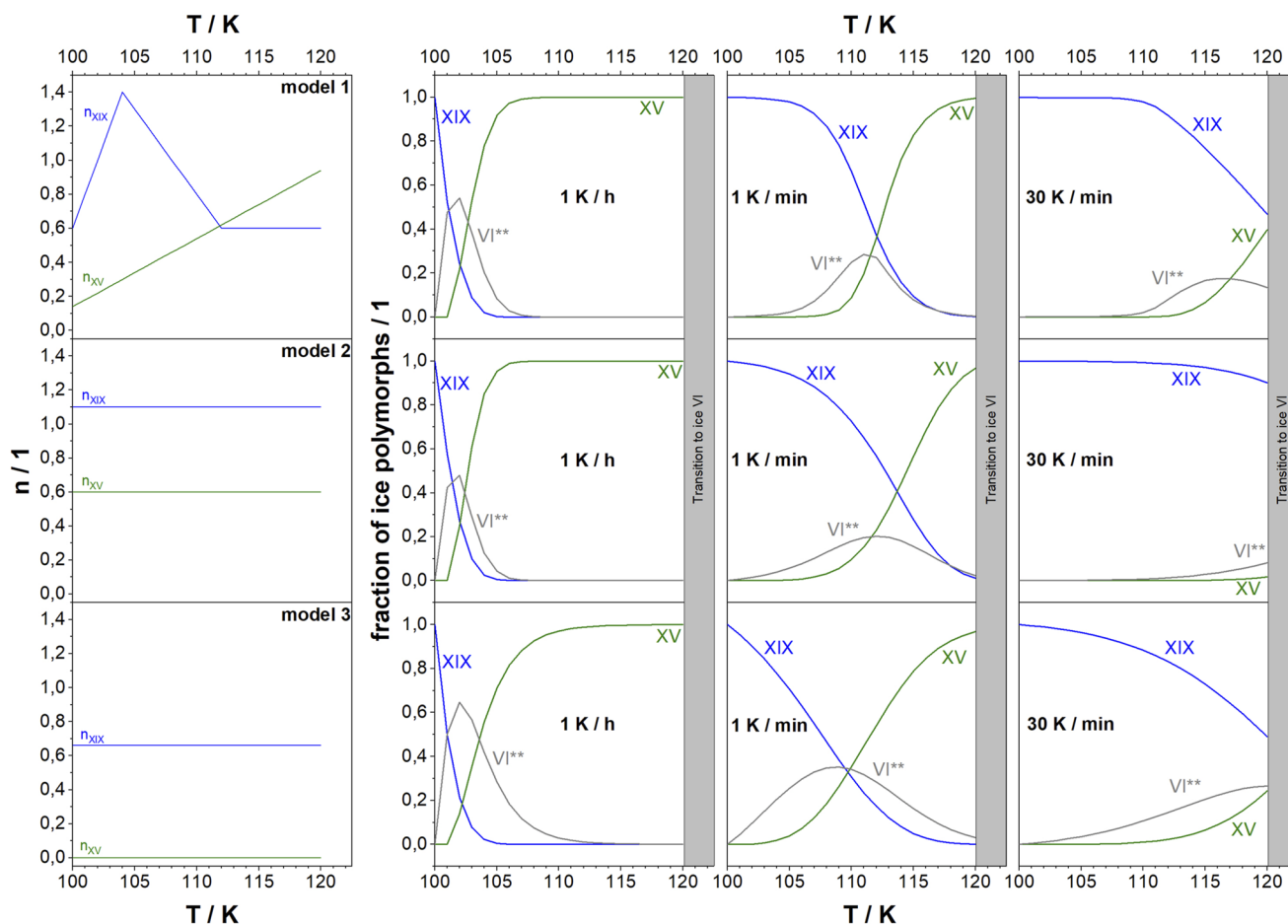


FIG. 5. Three different kinetic models for the reaction sequence ice XIX \rightarrow ice VI[‡] \rightarrow ice XV based on three different choices for the Avrami exponents n of ice XIX decay and ice XV build-up. The left column shows the choice of n , and the remaining three columns indicate fractions of ice polymorphs for slow (1 K/h), intermediate (1 K/min) and fast heating experiments of initial ice XIX. At 120 K, the transition to stable ice VI sets in, which is not considered in the present paper.

barely any ice XV appears. For instance, ice XIX is still a dominant ice polymorph in this model at 120 K but has fully disappeared in our calorimetry experiments. Since both of these models do not catch the time evolution of ice polymorphs in our experiments properly, we tried to find good exponents matching the experimental calorimetry and neutron diffraction observations upon heating. Best results are observed by using exponents of 2/3 for ice XIX decay and very small values, close to 0, for ice XV build-up. In addition, this model does not catch the observed behavior fully but at least catches the major observations properly: (i) ice XIX disappears above 100 K, (ii) ice XV appears near 110 K, and (iii) there is a build-up and decay of ice VI[‡] involving a significant fraction of above 20% for some time. We also tested the hypothesis of the Avrami exponent being coupled to the fraction of ice VI[‡] but did not obtain results superior to the ones shown in the third model. Possibly the model needs to additionally incorporate the ice XV decay to ice VI that takes place at the high temperature end to catch the physics of the order (ice XIX)–order (ice XV)–disorder(stable ice VI) transition sequence in full. Possibly the Avrami exponents are even heating-rate dependent—this could be the case if the Avrami exponent reflects domain growth kinetics, which in itself is limited by time and heating rate constraints. Such models are, however, detached from the “apparent” Avrami exponents obtained in the present work based on slow Raman heating experiments. It still remains a challenge to quantify the fractions of polymorphs as a function of widely varying heating rates. Unfortunately, we are lacking experimental determination of Avrami exponents similar to the study reported here but for fast heating experiments.

CONCLUSION

The polymorphic ice XIX → ice XV transition at ambient pressure represents the first and so far only order-to-order transition in the history of ice physics. As shown in our previous neutron diffraction work, the transition involves a reorientation of the subnetwork of deuterium atoms from one partly antiferroelectric arrangement to a different partly antiferroelectric arrangement.² The onset temperature for this transition has been established to be 100 K for hydrogenated ice XIX^{1,2,19} and 103 K for deuterated ice XIX² on the basis of our calorimetry experiments. According to the neutron diffraction patterns observed upon heating, the reaction path involves a disordered transition state, ice VI[‡]. In the calorimetry experiments, we observe a sequence of endotherm–exotherm–endotherm, which is consistent with the transition sequence ice XIX → ice VI[‡] → ice XV.^{1,2,19} For deuterated ice XIX, barely any ice XV appears in fast heating experiments, in contrast to slow heating experiments. The three ice phases were furthermore identified in terms of reorientation dynamics as observed through dielectric relaxation spectroscopy. In these experiments, we observed three different types of relaxation energies upon heating, thereby corroborating the observations in the neutron and x-ray diffraction as well as calorimetry experiments. A comparison of the observations in the different types of experiments needs to be taken with care since the heating rates differ widely: while the heating rates in the neutron diffraction and dielectric relaxation spectroscopy are on the order of 1 K h^{−1}, the heating rates in the calorimetry scans are usually 10 or 30 K min^{−1}, i.e., about 1000 times faster.

In the present work, we succeeded in measuring the reaction kinetics for both steps in the transition sequence and to establish kinetic parameters for them on the basis of Raman spectroscopy on deuterated samples (containing 5% H₂O). Previously, we have shown that hydrogenated ice VI, XV, and XIX can be easily distinguished through their Raman bands.¹ The presence of typical marker bands for each of the three polymorphs allows us to quantify fractions of individual polymorphs using a band superposition approach.²² Here, we extend this type of analysis from hydrogenated samples to deuterated samples and first report the Raman spectra and the isotope effects for all bands. We then conduct isothermal waiting experiments in the range between 98 and 119 K, in which we monitor first the ice XIX decay to ice VI[‡] and second the ice XV build-up from ice VI[‡]. The sigmoidal changes of ice fractions are then analyzed using the JMAK equation to extract rate constants *k* and Avrami exponents *n* for both ice XIX → ice VI[‡] and ice VI[‡] → ice XV. As seen in Table II and in the Arrhenius plot in Fig. 4, the latter is the rate-limiting step, which is about 20 times slower at 108 K. The very small and temperature-dependent Avrami exponents, especially at intermediate temperatures, suggest that both processes interfere with each other where the mechanism and rate of the transformation depend on the progress. The (apparent) activation energies for the two steps are 24 kJ mol^{−1} for deuterated ice XIX decay and 18 kJ mol^{−1} for ice XV formation. This is quite similar to the activation energies determined earlier by us for the protiated species using dielectric relaxation spectroscopy and suggests that similar processes are at the origin of dielectric relaxation in each phase and for the processes leading to the conversion. The process at the origin of both relaxation and conversion to a different H-ordered polymorph could be rotation of water dipoles. The 20-fold difference in reaction rates implies that ice VI[‡] is more rapidly formed than converted, thereby accumulating in the intermediate temperature range. This is the reason why, in fact, the transient disordered state can be resolved and characterized in the course of the heating experiment, as, e.g., in our diffraction, calorimetry, and relaxation spectroscopy work. The kinetic model in Fig. 5 taking both processes into account shows that in the intermediate temperature range, in fact, this accumulation is pronounced, with up to 20% of ice VI[‡] being present. In slow heating experiments (such as in the Raman experiment reported here and the neutron diffraction experiment reported earlier), ice VI[‡] peaks quite early, near 103–105 K, whereas in fast heating experiments (such as in our calorimetry experiments), ice VI[‡] persists to much higher temperatures. At fast heating rates, it is even possible that some ice VI[‡] remains even up to temperatures, where the transition of ice XV to stable ice VI sets in that is not considered in the present work. That is, some ice VI[‡] remains a transient species at 30 K min^{−1} up to the stability domain of ice VI, skipping the transition to ice XV. This is not the case for slow heating experiments at 1 K h^{−1}. This explains our earlier puzzling findings why barely any ice XV is observed upon rapid heating of deuterated ice XIX but significant amount in slow heating experiments.

SUPPLEMENTARY MATERIAL

The supplementary material shows an example for the superposition analysis (Fig. S1) and additional raw Raman data for the isothermal waiting experiments (Fig. S2).

ACKNOWLEDGMENTS

A.V.T. is the recipient of a DOC-fellowship of the Austrian Academy of Sciences ÖAW. We gratefully acknowledge financial support from the Centre for Molecular Water Sciences (CMWS) located at DESY in Hamburg.

AUTHOR DECLARATIONS

Conflict of Interest

The authors have no conflicts to disclose.

DATA AVAILABILITY

All raw data, including Raman time series and the kinetic models, are available from the corresponding author upon reasonable request.

REFERENCES

- ¹T. M. Gasser, A. V. Thoeny, L. J. Plaga, K. W. Köster, M. Etter, R. Böhmer, and T. Loerting, *Chem. Sci.* **9**(18), 4224–4234 (2018).
- ²T. M. Gasser, A. V. Thoeny, A. D. Fortes, and T. Loerting, *Nat. Commun.* **12**, 1128 (2021).
- ³L. del Rosso, M. Celli, F. Grazzi, M. Catti, T. C. Hansen, A. D. Fortes, and L. Ulivi, *Nat. Mater.* **19**(6), 663 (2020).
- ⁴K. Komatsu, S. Machida, F. Noritake, T. Hattori, A. Sano-Furukawa, R. Yamane, K. Yamashita, and H. Kagi, *Nat. Commun.* **11**, 464 (2020).
- ⁵V. B. Prakapenka, N. Holtgrewe, S. S. Lobanov, and A. F. Goncharov, *Nat. Phys.* **17**(11), 1233 (2021).
- ⁶T. Loerting, K. Winkel, M. Seidl, M. Bauer, C. Mitterdorfer, P. H. Handle, C. G. Salzmänn, E. Mayer, J. L. Finney, and D. T. Bowron, *Phys. Chem. Chem. Phys.* **13**(19), 8783–8794 (2011).
- ⁷S. Kawada, *J. Phys. Soc. Jpn.* **32**(5), 1442 (1972).
- ⁸Y. Tajima, T. Matsuo, and H. Suga, *J. Phys. Chem. Solids* **45**(11–12), 1135–1144 (1984).
- ⁹E. Whalley, J. B. R. Heath, and D. W. Davidson, *J. Chem. Phys.* **48**(5), 2362–2370 (1968).
- ¹⁰C. G. Salzmänn, P. G. Radaelli, A. Hallbrucker, E. Mayer, and J. L. Finney, *Science* **311**(5768), 1758–1761 (2006).
- ¹¹E. Whalley, D. W. Davidson, and J. B. R. Heath, *J. Chem. Phys.* **45**(11), 3976–3982 (1966).
- ¹²Y. Wang, K. Glazyrin, V. Roizen, A. R. Oganov, I. Chernyshov, X. Zhang, E. Greenberg, V. B. Prakapenka, X. Yang, S. Q. Jiang, and A. F. Goncharov, *Phys. Rev. Lett.* **125**(25), 255702 (2020).
- ¹³J. D. Bernal and R. H. Fowler, *J. Chem. Phys.* **1**(8), 515–548 (1933).
- ¹⁴B. Kamb, *Science* **150**, 205–209 (1965).
- ¹⁵C. G. Salzmänn, P. G. Radaelli, E. Mayer, and J. L. Finney, *Phys. Rev. Lett.* **103**(10), 105701 (2009).
- ¹⁶R. Yamane, K. Komatsu, J. Gouchi, Y. Uwatoko, S. Machida, T. Hattori, H. Ito, and H. Kagi, *Nat. Commun.* **12**, 1129 (2021).
- ¹⁷A. Polian and M. Grimsditch, *Phys. Rev. Lett.* **52**(15), 1312–1314 (1984).
- ¹⁸M. Millot, F. Coppari, J. R. Rygg, A. Correa Barrios, S. Hamel, D. C. Swift, and J. H. Eggert, *Nature* **569**(7755), 251–255 (2019).
- ¹⁹T. M. Gasser, A. V. Thoeny, V. Greussing, and T. Loerting, *J. Phys. Chem. B* **125**(42), 11777–11783 (2021).
- ²⁰C. G. Salzmänn, J. S. Loveday, A. Rosu-Finsen, and C. L. Bull, *Nat. Commun.* **12**, 3162 (2021).
- ²¹T. C. Hansen, *Nat. Commun.* **12**, 3161 (2021).
- ²²A. V. Thoeny, T. M. Gasser, and T. Loerting, *Phys. Chem. Chem. Phys.* **21**(28), 15452–15462 (2019).
- ²³Y. P. Khanna and T. J. Taylor, *Polym. Eng. Sci.* **28**(16), 1042–1045 (1988).
- ²⁴J. J. Shephard and C. G. Salzmänn, *Chem. Phys. Lett.* **637**, 63–66 (2015).
- ²⁵T. F. Whale, S. J. Clark, J. L. Finney, and C. G. Salzmänn, *J. Raman Spectrosc.* **44**(2), 290–298 (2013).
- ²⁶C. Haas and D. F. Hornig, *J. Chem. Phys.* **32**(6), 1763–1769 (1960).